Int J Fract
DOI 10.1007/s10704-011-9593-y

ORIGINAL PAPER

An XFEM/Spectral element method for dynamic crack propagation

Z. L. Liu · T. Menouillard · T. Belytschko

Received: 28 October 2010 / Accepted: 8 February 2011

Abstract A high-order extended finite element method based on the spectral element method for the simulation of dynamic fracture is developed. The partition of unity for the discontinuous displacement is constructed by employing p order spectral element. This method shows great advantages in the simulations of moving crack and mixed mode crack. The numerical oscillations are effectively suppressed and the accuracy of computed stress intensity factors and crack path are improved markedly. Furthermore the simulation results show that p-refinement is more effective in improving the stress contour near the crack tip than h-refinement. The well known form of the explicit central difference method is used and the critical time step for this method is investigated. We find that by using lumped mass matrix the critical time step Δt_c for this high-order extended finite element is almost independent of the crack position.

Keywords XFEM · Spectral element · Dynamic fracture

Z. L. Liu · T. Menouillard · T. Belytschko (✉)
Department of Mechanical Engineering, Northwestern University, 2145 Sheridan Road, Evanston, IL 60208-3111, USA
e-mail: tedbelytschko@northwestern.edu

Z. L. Liu
e-mail: zhanli-liu@northwestern.edu

T. Menouillard
e-mail: t-menouillard@northwestern.edu

1 Introduction

Classical finite element strategies for dynamic crack propagation simulation are limited because of the evolution of the topology due to the crack. They require remeshing during crack propagation, and also a projection. To adapt the standard finite element method to fracture computation, the extended finite element method (XFEM) has been developed by Belytschko and Black (1999), Moës et al. (1999), which completely avoids remeshing. The XFEM method is based on the partition of unity pioneered by Melenk and Babuška (1996), whereby specific functions are used to describe the physical behavior in subdomains of the problem. A major step in the applications of these concepts to fracture is Moës et al. (1999) who used a Heaviside enrichment function along the crack to describe the discontinuous displacement. Belytschko et al. (2003) developed a method for dynamic crack propagation with loss of hyperbolicity as a propagation criterion. They developed a special element with linear crack opening at the tip. Song et al. (2006) developed a phantom node method based on the Hansbo and Hansbo (2004) formulation for crack and shear band propagation. This approach has some advantages, but the basis functions are identical to XFEM in Areias and Belytschko (2005). This method was also extended to shells by Song and Belytschko (2009) and 3D fracture by Duan et al. (2009). All these studies are limited to low-order finite elements.

Published online: 02 March 2011

One difficulty with low-order finite elements, both in the context of XFEM and other application to dynamic problems, is that it sometimes does not have the desired accuracy. It exhibits the rather marked wave oscillations and low-order finite element method. The numerical oscillations are strongly amplified during the dynamic crack propagation. Recent work on the time-dependent tip enrichment (Menouillard et al. 2010; Réthoré et al. 2005), with a smooth release of the crack tip element (Menouillard and Belytschko 2009) and on the enrichment with mesh-free method (Menouillard et al. 2010) showed some improvement in the accuracy of the stress intensity factors. However, Areias and Belytschko (2005), Réthoré et al. (2005) and Song et al. (2006) noted that, for low-order elements the increase in accuracy that accrues to including partially cracked elements in the formulation and implementation is quite marginal.

The spectral elements, originally proposed by Patera for fluid dynamics (Patera 1984), have become popular for wave propagation (Capdeville et al. 2003; Komatitsch and Tromp 1999; Komatitsch and Vilotte 1998; Seriani and Oliveira 2007) because they are able to deliver significantly better accuracy as compared to standard finite element methods (Padovani et al. 1994).

This high-order numerical technique combines the high accuracy of spectral methods with the flexibility of finite elements. Furthermore, p-refinement of spectral elements is very easy to implement. The spectral element method for elastic wave propagation is well known for quadrilateral element meshes with shape functions based on Chebyshev or Legendre orthogonal polynomials (Komatitsch and Tromp 1999), as well as for triangular grids (Mercerat et al. 2006). Recently, Legay et al. (2005) applied XFEM to spectral elements to model the static discontinuities, e.g. the inclusion problems, and static cracks.

In this work we develop a high-order extended finite element method using spectral elements. The objective is to increase accuracy and decrease the numerical oscillations in the modeling of dynamic fracture. This method shows many advantages in the simulation of moving crack. The computed crack paths and stress intensity factors converge more rapidly. The numerical oscillations are effectively suppressed during the crack propagation.

This paper is organized as follows. Section 2 describes the approximation of the continuous and discontinuous displacement fields in spectral element. Section 3 introduces and develops the space discretization. Section 4 presents the time discretization corresponding to the central difference method and its stability. The fracture mechanics is developed in Sect. 5. Section 6 deals with different numerical applications and the improvements in this method are demonstrated. Section 7 discusses this approach and gives some conclusions.

2 Methodology

2.1 Enriched displacement fields

Consider a body Ω_0 with its boundary Γ_0 and a crack on a surface Γ_c^0 (a line in two dimensions) in the reference configuration as shown in Fig. 1. The material coordinates are denoted by $\mathbf{X}$ and the motion is described by $\mathbf{x} = \Phi(\mathbf{X}, t)$ where $\mathbf{x}$ are the spatial coordinates and t the time. In the current configuration, the image of Ω_0 is Ω. We define the location of the discontinuity Γ_c (i.e. the crack) implicitly by a level set; in particular, we choose the signed distance function f so that $f(\mathbf{x}) = 0$ gives the discontinuity (crack) surface. For the case where the discontinuity ends within the domain, we define the location of the end of the discontinuity by constructing another function $g(\mathbf{x}, t)$such that $g(\mathbf{x}, t) > 0$ in the subdomain cut by Γ_c as shown in Fig. 2. The location of the discontinuity is then given by

$$\Gamma_c = \{\mathbf{x} \in \Omega_0 | f(\mathbf{x}) = 0 \quad \text{and} \quad g(\mathbf{x}, t) > 0\} \tag{1}$$

The construction of the approximation $\mathbf{u}^h$ for the displacement field $\mathbf{u}(\mathbf{x}, t)$ is based on an additive

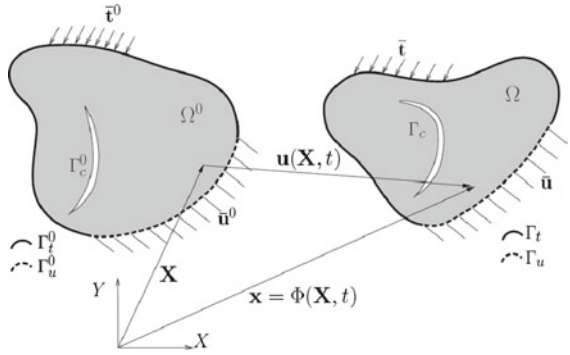

Fig. 1 A two-dimensional body with a discontinuity and its representation in the initial and the current domains

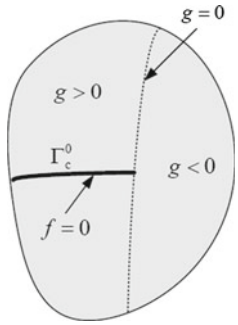

Fig. 2 A two-dimensional discontinuity representation by two implicit functions $f(\mathbf{x})$ and $g(\mathbf{x}, t)$

decomposition of the function into its continuous and discontinuous parts (Moës et al. 1999):

$$\mathbf{u}^h(\mathbf{x}, t) = \mathbf{u}^{\text{cont}}(\mathbf{x}, t) + \mathbf{u}^{\text{cut}}(\mathbf{x}, t) + \mathbf{u}^{\text{tip}}(\mathbf{x}, t) \tag{2}$$

where $\mathbf{u}^{\text{cont}}$ is the continuous part of the displacement, $\mathbf{u}^{\text{cut}}$ the discontinuous part along the crack and $\mathbf{u}^{\text{tip}}$ the enriched displacement near the crack tip. We now approximate the continuous part of $\mathbf{u}^h$ by standard spectral shape functions and the discontinuous part by the local partition of unity, respectively:

$$\mathbf{u}^{\text{cont}}(\mathbf{x}, t) = \sum_{I \in N} N_I^p(\mathbf{x}) \mathbf{u}_I(t) \tag{3}$$

where N is the total number of nodes in the model, $N_I^p(\mathbf{x})$ is the spectral shape function of order p, $\mathbf{u}_I$ are the nodal values.

The discontinuity along the crack surface, i.e. the second term in Eq. (2), is modeled by

$$\mathbf{u}^{\text{cut}}(\mathbf{x}, t) = \sum_{I \in N^{\text{cut}}} N_I^p(\mathbf{x}) H(f(\mathbf{x})) \mathbf{a}_I(t) \tag{4}$$

where $\mathbf{a}_I$ are additional degrees of freedom, often known as enriched degrees of freedom and $H(\cdot)$ is the Heaviside step function given by:

$$H(S) = \begin{cases} 1 & S \geq 0 \\ -1 & S < 0 \end{cases} \tag{5}$$

and N^{cut} is the set of enriched nodes associated with the discontinuity. It includes the nodes of elements which are cut by the crack Γ_c. An example of the enrichment scheme is shown in Fig. 3, the set of nodes N^{cut} is represented by blue squares.

The tip enrichment, the third term in Eq. (2), is of the form

$$\mathbf{u}^{\text{tip}}(\mathbf{x}, t) = \sum_{I \in N^{\text{tip}}} N_I^p(\mathbf{x}) \Phi(\mathbf{x}) \mathbf{b}_I(t) \tag{6}$$

where $\mathbf{b}_I$ are the parameters associated with the tip enrichment and N^{tip} is the set of nodes in the crack-tip influence domain which is centered at crack tip as shown in Fig. 3. The nodes in N^{tip} are denoted by red circles in Fig. 3.

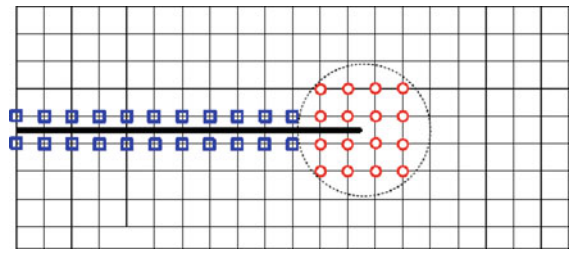

Fig. 3 Definition of the node sets N^{cut} and N^{tip}. The nodes in N^{cut} are represented by blue squares and the nodes in N^{tip} are represented by red circles

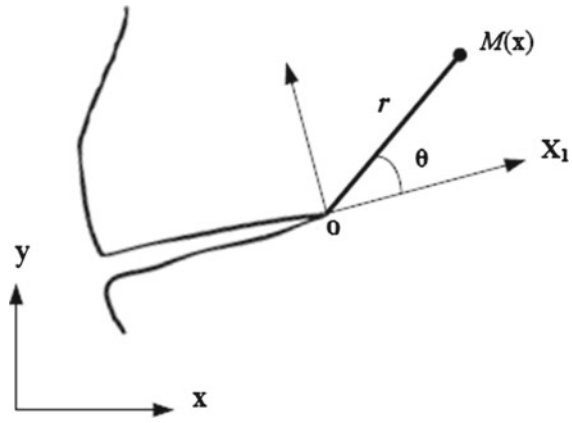

Fig. 4 Cartesian and polar coordinates used near crack tip

The following tip enrichment function $\Phi(\mathbf{x})$ is used in our study:

$$\Phi(\mathbf{x}) = \sqrt{r} \sin\left(\frac{\theta}{2}\right) \tag{7}$$

where r and θ define the crack-tip based local polar coordinates as shown in Fig. 4. This enrichment is the standard singular crack-tip field for linear elasticity and it works well in enriching the crack-tip nodes (Menouillard et al. 2010). Other functions can be used to improve the enrichment around the crack tip (Fleming et al. 1997; Moës et al. 1999).

Now the displacement can be expressed as:

$$\mathbf{u}(\mathbf{x}) = \sum_{I \in N} N_I^p(\mathbf{x}) \mathbf{u}_I + \sum_{J \in N^{\text{cut}}} N_J^p(\mathbf{x}) H(f(\mathbf{x})) \mathbf{a}_J(t) + \sum_{K \in N^{\text{tip}}} N_K^p(\mathbf{x}) \Phi(\mathbf{x}) \mathbf{b}_K(t) \tag{8}$$

In our implementation, the distance function $f(\mathbf{x})$ can be approximated as:

$$f(\mathbf{x}) = \sum_{I \in N^{\text{cut}}} N_I^p(\mathbf{x}) f_I(\mathbf{x}_I) \tag{9}$$

The interpolation is only constructed in the influence domain given by N^{cut}.

2.2 Spectral approximation

We use the spectral elements (SE) of Patera (1984) with a formulation based on Karniadakis and Sherwin (1999). The element employs spaced nodes corresponding to the zeros of the Chebyshev or Legendre polynomials, called in this work a Chebyshev-Gauss point repartition. The pth order Chebyshev polynomial is

$$T_p(x) = \cos(p\theta) \quad \text{with} \quad \theta = \arccos x \quad \text{and} \quad x \in [-1, 1] \tag{10}$$

Nodal coordinates in the element are chosen such that the derivative T_p' of T_p at x_I is zero:

$$T_p'(x_I) = 0, \ I = 1, 2, \ldots, p-1 \quad \text{and} \quad x_0 = 1, x_P = 1 \tag{11}$$

One can then show that

$$x_I = -\cos\frac{I\pi}{p}, \ \text{for } I \in \{0, 1, 2, \ldots, p\} \tag{12}$$

Note that this repartition of nodes allows us to write the shape function in terms of Chebyshev polynomials (Patera 1984)

$$N_I^{1D}(x) = \frac{(-1)^{I+p}(x^2-1)T_P'(x)}{c_I p^2 (x - x_I)} = \frac{2}{p}\sum_{J=0}^{p}\frac{1}{c_I c_J} T_J(x_I) T_J(x) \tag{13}$$

where $c_I = 2$ if I is 0 or p, $c_I = 1$ otherwise. In two dimensions, the same nodal distribution is taken in each direction. The following notation is used for node I, J:

$$\mathbf{x}_{I,J} = (x_I, y_J) = \left(-\cos\frac{I\pi}{p}, -\cos\frac{J\pi}{p}\right) \tag{14}$$

where I and J vary from 0 to p. The shape functions are obtained by a tensor product of the one-dimensional shape functions $N_I^{1D}(x)$

$$N_{IJ}(\mathbf{x}) = N_{IJ}(x, y) = N_I^{1D}(x) N_J^{1D}(y) \tag{15}$$

Figure 5 shows the second and third order spectral element and their nodes.

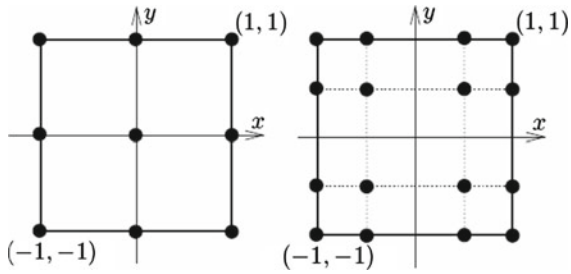

Fig. 5 Second and third order spectral elements and node repartition

3 Space discretization

3.1 Governing equation

We consider a two-dimensional small deformation dynamic problem. The strong form of the linear momentum equation is

$$\nabla \cdot \boldsymbol{\sigma} + \rho\mathbf{b} - \rho\ddot{\mathbf{u}} = 0 \quad \text{in } \Omega \tag{16}$$

where $\boldsymbol{\sigma}$ is Cauchy stress tensor, ρ is the initial mass density, $\mathbf{b}$ is the body force vector.

The boundary conditions are

$$\mathbf{u} = \bar{\mathbf{u}} \quad \text{on } \Gamma_u \tag{17}$$

$$\boldsymbol{\sigma} \cdot \mathbf{n} = \bar{\mathbf{t}} \quad \text{on } \Gamma_t \tag{18}$$

$$\boldsymbol{\sigma} \cdot \mathbf{n} = 0 \quad \text{on } \Gamma_c \tag{19}$$

where $\mathbf{n}$ is the normal to the indicated boundary, $\bar{\mathbf{u}}$ is the applied displacement on the Dirichlet boundary Γ_u, $\bar{\mathbf{t}}^0$ is the applied traction on the Neumann boundary Γ_t and the crack surface Γ_c is assumed traction free; $\Gamma_u \cup \Gamma_t \cup \Gamma_c = \Gamma$, $\Gamma_u \cap \Gamma_t = \emptyset$. Figure 1 presents the different domains and boundaries.

3.2 Finite element formulation

The discrete equations are constructed by the standard Galerkin procedures. The admissible space for the displacement fields is defined as follows:

$$u = \Big\{\mathbf{u}(\mathbf{x}, t) \in C^0 | \mathbf{u}(\mathbf{x}, t) = \bar{\mathbf{u}}(t) \text{ on } \Gamma_u, \ \mathbf{u} \text{ discontinuous on crack surface}\Big\} \tag{20}$$

$$u_0 = \Big\{\delta\mathbf{u}(\mathbf{x}, t) \in C^0 | \delta\mathbf{u}(\mathbf{x}, t) = 0 \text{ on } \Gamma_u, \ \delta\mathbf{u} \text{ discontinuous on crack surface}\Big\} \tag{21}$$

The weak form for the momentum equation is:

$$\int_\Omega \delta\mathbf{u}\cdot\rho\ddot{\mathbf{u}}d\Omega = \int_\Omega \delta\mathbf{u}\cdot\rho\mathbf{b}d\Omega + \int_{\Gamma_t}\delta\mathbf{u}\cdot\bar{\mathbf{t}}d\Omega - \int_\Omega \frac{\partial\delta\mathbf{u}}{\partial\mathbf{x}}:\boldsymbol{\sigma}d\Omega \tag{22}$$

Then substituting the displacement field (8) into the weak form Eq. (22) gives (see reference Belytschko et al. 2000 for details):

$$\mathbf{M}_{IJ}\ddot{\mathbf{u}}_J^h = \mathbf{f}_I^{\text{ext}} - \mathbf{f}_I^{\text{int}} \tag{23}$$

and the remaining terms are defined below

$$\ddot{\mathbf{u}}_I^h = \begin{Bmatrix}\ddot{\mathbf{u}}_I\\ \ddot{\mathbf{a}}_I\\ \ddot{\mathbf{b}}_I\end{Bmatrix},\ \mathbf{f}_I^{\text{int}} = \begin{Bmatrix}\mathbf{f}_I^{u,\text{int}}\\ \mathbf{f}_I^{a,\text{int}}\\ \mathbf{f}_I^{b,\text{int}}\end{Bmatrix},\quad \mathbf{f}_I^{\text{ext}} = \begin{Bmatrix}\mathbf{f}_I^{u,\text{ext}}\\ \mathbf{f}_I^{a,\text{ext}}\\ \mathbf{f}_I^{b,\text{ext}}\end{Bmatrix} \tag{24}$$

where

$$\mathbf{f}_I^{u,\text{int}} = \int_\Omega \mathbf{B}_{uI}^{\mathrm{T}}\boldsymbol{\sigma}d\Omega,\ \mathbf{f}_I^{a,\text{int}} = \int_{\Omega_H}\mathbf{B}_{aI}^{\mathrm{T}}\boldsymbol{\sigma}d\Omega_H,\ \mathbf{f}_I^{b,\text{int}} = \int_{\Omega_S}\mathbf{B}_{bI}^{\mathrm{T}}\boldsymbol{\sigma}d\Omega_S \tag{25}$$

where

$$\mathbf{B}_{uI} = \begin{bmatrix} N_{I,x}^p & 0\\ 0 & N_{I,y}^p\\ N_{I,y}^p & N_{I,x}^p\end{bmatrix},$$

$$\mathbf{B}_{aI} = \begin{bmatrix} N_{I,x}^p H(f(\mathbf{x})) & 0\\ 0 & N_{I,y}^p H(f(\mathbf{x}))\\ N_{I,y}^p H(f(\mathbf{x})) & N_{I,x}^p H(f(\mathbf{x}))\end{bmatrix} \tag{26}$$

$$\mathbf{B}_{bI} = \begin{bmatrix} N_I^p\Phi_{,x} + N_{I,x}^p\Phi & 0\\ 0 & N_I^p\Phi_{,y} + N_{I,y}^p\Phi\\ N_I^p\Phi_{,y} + N_{I,y}^p\Phi & N_I^p\Phi_{,x} + N_{I,x}^p\Phi\end{bmatrix} \tag{27}$$

The strain can be expressed by strain-displacement relation:

$$\boldsymbol{\varepsilon}(\mathbf{u}(\mathbf{x})) = \boldsymbol{\varepsilon}\left(\mathbf{u}^{\text{cont}} + \mathbf{u}^{\text{cut}} + \mathbf{u}^{\text{tip}}\right) = \mathbf{B}_{uI}\mathbf{u}_I + \mathbf{B}_{aI}\mathbf{a}_I + \mathbf{B}_{bI}\mathbf{b}_I \tag{28}$$

Then Cauchy stress $\boldsymbol{\sigma}$ in Eq. (25) is given by Hooke's law:

$$\boldsymbol{\sigma} = \mathbf{C}:\boldsymbol{\varepsilon} \tag{29}$$

The mass matrix is given by:

$$\mathbf{M}_{IJ}^{uu} = \int_\Omega \rho N_I N_J d\Omega,\quad \mathbf{M}_{IJ}^{aa} = \int_\Omega \rho N_I N_J H^2(f(\mathbf{x}))d\Omega \tag{30}$$

$$\mathbf{M}_{IJ}^{ua} = \int_\Omega \rho N_I N_J H(f(\mathbf{x}))d\Omega,\quad \mathbf{M}_{IJ}^{bb} = \int_\Omega \rho N_I N_J \Phi^2(\mathbf{x})d\Omega \tag{31}$$

$$\mathbf{M}_{IJ}^{ub} = \int_\Omega \rho N_I N_J \Phi(\mathbf{x})d\Omega,\quad \mathbf{M}_{IJ}^{ab} = \int_\Omega \rho N_I N_J H(f(\mathbf{x}))\Phi(\mathbf{x})d\Omega \tag{32}$$

In the simulations, only the current crack tip is enriched with enrichment function. When the crack tip reaches a new element, the enrichment type of some nodes of this element changes, from Φ to H, and the degrees of freedoms corresponding to Heaviside function have to be initiated (Menouillard et al. 2010; Réthoré et al. 2005). The continuity of the displacement and velocity is chosen for the condition to be verified to initialize the new discontinuous degrees of freedom. With this strategy, the initial value of the new discontinuous enrichment (i.e., corresponding to the H degrees of freedom) will not be taken as zero.

3.3 Integration scheme

For elements containing the crack, the integrals in Eq. (25) cannot be evaluated by standard quadrature methods since the integrand is discontinuous. For this purpose, the element cut by the crack is subdivided into subdomains Ω^{e+} and Ω^{e-} where

$$\Omega^{e+} = \Omega^e \cap (f(\mathbf{x}) > 0)\\ \Omega^{e-} = \Omega^e \cap (f(\mathbf{x}) < 0) \tag{33}$$

The subdomains Ω^{e+} and Ω^{e-} are approximated by simple patterns of triangles (Chessa et al. 2003; Moës et al. 1999) or trapezoids (Fish and Belytschko 1990), then standard quadrature is used over these subdomains. It should be noted that in the subdomain integration for triangular elements, we need to map the quadrature points of the high-order quadrilateral spectral elements to the triangles, see Reference Legay et al. (2005) for details.

4 Time integration and stable time step

The well known form of the explicit central difference method is used (see Reference Belytschko et al. 2000 for a description). The stability condition for the central difference method restricts the time step to be smaller than a critical time step Δt_c:

$$\Delta t \leq \Delta t_c = \min_e \left(\Delta t_c^e\right) \tag{34}$$

where Δt_c^e is the critical time step of element e, which is calculated by:

$$\Delta t_c^e = \frac{2}{\omega_{\max}^e} \tag{35}$$

where $\omega_{\max}^e$ denotes the maximum frequency of element e obtained from the eigenvalue problem:

$$\det\left(\mathbb{K}^e - \omega^2 \mathbb{M}^e\right) = 0 \tag{36}$$

We first consider a 1D cracked element of section A, length L, Young's modulus E and mass density ρ as an example to decide the stable time step in this high-order XFEM method. For a standard 1D two-nodes element (without discontinuity), the critical time step for the lumped mass matrix is $\frac{L}{c}$ $\left(c = \sqrt{\frac{E}{\rho}}\right.$ is wave velocity$\left.\right)$. This time step is chosen as the reference critical time step Δt_c^0 in the following.

The critical time steps for both lumped mass and consistent mass are investigated. In our implementation, the mass matrix corresponding to the standard degrees of freedom $\mathbf{u}_I$ are lumped by a row-sum procedure. The mass matrix linked to the enrichment parameters $\mathbf{a}_I$ and $\mathbf{b}_I$ is diagonalized as described in References Elguedj et al. (2009), Menouillard et al. (2006), Menouillard et al. (2008):

$$\text{for } \mathbf{a}_I: \quad m_{\text{diag}} = \frac{m}{n_{\text{nodes}}} \frac{1}{\text{mes}(\Omega_{\text{el}})} \int_{\Omega_{\text{el}}} H^2(\mathbf{x}) d\Omega \tag{37}$$

$$\text{for } \mathbf{b}_I: \quad m_{\text{diag}} = \frac{1}{\sum_K \Phi^2(\mathbf{x}_K)} \int_{\Omega_{\text{el}}} \rho \Phi^2(\mathbf{x}) d\Omega \tag{38}$$

where Ω_{el} is the element being considered, m its mass, $\text{mes}(\Omega_{\text{el}})$ its length (in 1D), area (in 2D), or volume (in 3D), n_{nodes} the number of nodes of Ω_{el}, and H is Heaviside step function and Φ the tip enrichment function.

For the explicit time integration in high-order XFEM, the lumped mass matrix has several advantages compared to the consistent mass matrix. It should be noted that a diagonal mass matrix is usually used in explicit schemes. The advantage is to speed up the computation, and use less memory by storing only vectors instead of matrices. This can be seen in the following comparisons.

Table 1 Critical time steps in a 1D spectral element without discontinuity

Spectral element order	Critical time step (normalized by Δt_c^0)	
	Lumped mass	Consistent mass
1	1	0.577
2	0.408	0.258
3	0.196	0.153
4	0.117	0.102

First we calculate the critical time step for 1D spectral element without containing discontinuity. The results for both lumped mass and consistent mass are given in Table 1. The critical time step Δt_c is normalized by the reference critical time step Δt_c^0.

Now let us estimate the critical time step for 1D spectral element containing a discontinuity. As shown in Fig. 6, the discontinuity at location S is described by a generalized Heaviside function centered in S:

$$H(x - S) = \begin{cases} 1 & x \geq S \\ -1 & x < S \end{cases} \tag{39}$$

For both lumped mass and consistent mass, the critical time steps for the element as the location S of the discontinuity are given in Fig. 6 for different spectral element orders. The lumped mass matrix is obtained by the scheme described above. As shown in Fig. 6, for the higher order spectral elements with lumped mass, Δt_c does not change much with S, even when the discontinuity approaches either end of the element. But for the consistent mass, the critical time step Δt_c for higher order spectral elements decreases to zero as the discontinuity approaches one end of the element, so the stability of the explicit central difference scheme for the mesh can not be guaranteed. According to Fig. 6, $\Delta t_c = 10 \sim 20\% \Delta t_c^0$ is chosen in the simulations below.

Note that for element with linear shape function, e.g. constant strain element such as 3-node linear element (Belytschko et al. 2003), 4-node element with one quadrature point and hourglass control (Song et al. 2006), the critical time step for the cracked element is the same as that of the continuum element.

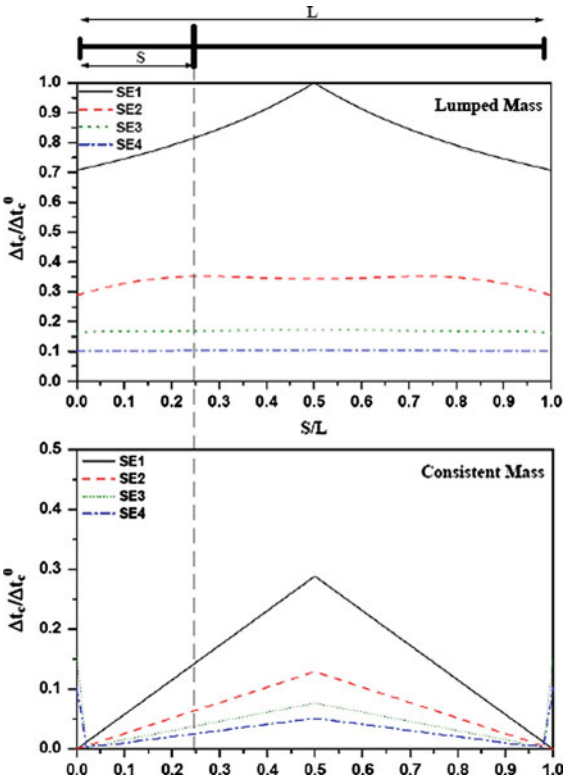

Fig. 6 Critical time steps as a function of the location of the discontinuity in a 1D spectral element

5 Fracture mechanics

5.1 Stress intensity factors

The dynamic stress intensity factors K_I and K_{II} are defined by asymptotic behavior of the stress near crack tip (see Reference Freund 1990 for details and references therein):

$$K_I = \lim_{r\to 0} \sqrt{2\pi r}\sigma_{yy} \tag{40}$$

$$K_{II} = \lim_{r\to 0} \sqrt{2\pi r}\sigma_{xy} \tag{41}$$

The relation between the energy release rate and the stress intensity factor is given by:

$$G = \frac{1-\nu^2}{E}\left[\beta_1(\dot{a})K_I^2 + \beta_2(\dot{a})K_{II}^2\right] \tag{42}$$

where E denotes the Young's modulus, ν the Poisson's ratio, $\dot{a}$ the crack velocity. β_i $(i = 1, 2)$ are the universal functions defined by:

$$\beta_i(\dot{a}) = \frac{\dot{a}^2\alpha_i}{(1-\dot{a})c_2^2 D} \tag{43}$$

$$\alpha_i = \sqrt{1-\frac{\dot{a}^2}{c_i^2}} \tag{44}$$

$$D(\dot{a}) = 4\alpha_1\alpha_2 - \left(1+\alpha_2^2\right)^2 \tag{45}$$

where c_1 and c_2 are, respectively dilatational and shear wave speed, and are given as a function of Lamé coefficients and the density as:

$$c_1 = \sqrt{\frac{\lambda+2\mu}{\rho}}, \quad c_2 = \sqrt{\frac{\mu}{\rho}} \tag{46}$$

The computations of K_I and K_{II} are based on the auxiliary fields near crack tip, the J-integral (Rice 1968) and the interaction integral. Details of the interaction integral can be found in References Freund (1990), Krysl and Belytschko (1999).

The stress intensity factors K_I and K_{II} are evaluated using a domain independent integral I_{int} and a virtual crack extension $\mathbf{q}$ by (see References Attigui and Petit 1997; Réthoré et al. 2005 for details):

$$\begin{aligned} I_{int} = &-\int_\Omega \left(\boldsymbol{\sigma}^{\text{aux}} : \nabla\mathbf{u} - \rho\dot{\mathbf{u}}\dot{u}^{\text{aux}}\right) \text{ div}\,(\mathbf{q})d\Omega \\ &+\int_\Omega \boldsymbol{\sigma}^{\text{aux}} : (\nabla\mathbf{u}\nabla\mathbf{q}) + \boldsymbol{\sigma} : \left(\nabla\mathbf{u}^{\text{aux}}\nabla\mathbf{q}\right) d\Omega \\ &+\int_\Omega \text{div}\left(\boldsymbol{\sigma}^{\text{aux}}\right)\nabla\mathbf{u}(\mathbf{q}) + \rho\ddot{\mathbf{u}}\nabla\mathbf{u}^{\text{aux}}d\Omega \\ &+\int_\Omega \rho\dot{\mathbf{u}}^{\text{aux}}\nabla\dot{\mathbf{u}}(\mathbf{q}) + \rho\dot{\mathbf{u}}\nabla\dot{\mathbf{u}}^{\text{aux}}(\mathbf{q})d\Omega \end{aligned} \tag{47}$$

where $\boldsymbol{\sigma}^{\text{aux}}$ and $\mathbf{u}^{\text{aux}}$ are auxiliary stress and displacement fields. The norm of vector $\mathbf{q}$, parallel to the crack, is defined by

$$q = \begin{cases} 0 & \text{outside the surface } S_1 \cup S_2 \\ \|q\| = 1 & \text{inside the surface } S_1 \\ \|q\| & \text{linear inside the surface } S_2 \end{cases} \tag{48}$$

where S_1 and S_2 are surface defined near the crack tip. Figure 7 shows the surfaces S_1 and S_2, and presents the direction and norm of the virtual extension field $\mathbf{q}$ near the crack tip.

Then this integral is

$$\begin{aligned} I_{int} = &\frac{2\left(1-\nu^2\right)}{E}\left[\beta_1(\dot{a})K_I K_I^{\text{aux}}\right. \\ &\left.+\beta_2(\dot{a})K_{II}K_{II}^{\text{aux}}\right] \end{aligned} \tag{49}$$

The different stress intensity factors are estimated through an appropriate choice of $\mathbf{u}^{\text{aux}}$: i.e. $K_I^{\text{aux}} = 1$ and $K_{II}^{\text{aux}} = 0$ for the determination of K_I, and $K_I^{\text{aux}} = 0$ and $K_{II}^{\text{aux}} = 1$ for the determination of K_{II}.

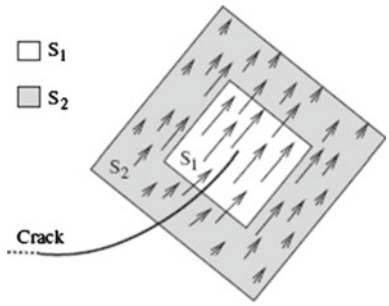

Fig. 7 Direction and norm of virtual extension field **q**

5.2 Crack velocity law

From the knowledge of dynamic stress intensity factors, the equivalent dynamic stress intensity factor $K_{\theta\theta}$ is defined by:

$$K_{\theta\theta} = \cos^3\left(\frac{\theta_c}{2}\right) K_I - \frac{3}{2}\cos\left(\frac{\theta_c}{2}\right)\sin\theta_c K_{II} \quad (50)$$

where θ_c is the direction of the crack driven by the maximum hoop stress criterion as:

$$\theta_c = 2\arctan\left[\frac{1}{4}\left(\frac{K_I}{K_{II}} - \mathrm{sign}(K_{II}) \times\sqrt{8+\left(\frac{K_I}{K_{II}}\right)^2}\right)\right] \quad (51)$$

Freund (1990) developed a relation between the dynamics energy release rate and the crack velocity. Freund and Douglas (1982) and Rosakis and Freund (1982) have linked experimentally the crack velocity to the stress intensity factors through the relation explained by Freund (1990):

$$\dot{a} = \begin{cases} 0 & \text{if } K_{\theta\theta} < K_{IC}, \\ c_r\left(1-\left(\frac{K_{IC}}{K_{\theta\theta}}\right)^2\right) & \text{otherwise.} \end{cases} \quad (52)$$

So a crack increment in the explicit algorithm is defined by $\Delta a = \dot{a}\Delta t$, where Δt is the time step size.

6 Numerical results

In this section, we present several numerical examples of stationary cracks under dynamic load and dynamic crack growth under the assumption of plain strain two-dimensional elasticity.

6.1 Stationary and moving mode I crack

The example considered in this section is an infinite plate with a semi infinite crack loaded by a tensile stress perpendicular to the crack surface.

A schematic of this problem is shown in Fig. 8. A uniform traction $\sigma_0(t)$ is applied to the top edge. The plate dimensions are: the length $L = 10\,\mathrm{m}$, the initial crack length is $a = 5\,\mathrm{m}$, and the vertical position of the crack is $h = 2\,\mathrm{m}$. A mesh of 61×120 spectral elements is used to define the model. Since the specimen is finite, we stop the simulation when the reflected wave from the edge reaches the crack tip, i.e. $t \leq 3t_c = 3h/c_1$ (c_1 is the dilatation wave speed).

The material properties are: Young's modulus $E = 210\,\mathrm{GPa}$, Poisson's ratio $\nu = 0.3$ and the density $\rho = 8,000\,\mathrm{kg/m^3}$ and plane strain conditions are used.

The loading $\sigma_0(t)$ is defined by

$$\sigma_0(t) = \sigma^* f_n(t) \quad (53)$$

where $\sigma^* = 5 \times 10^5\,\mathrm{Pa}$ and the laws $f_n(t)$ are defined by:

$$f_0(t) = \begin{cases} 0 & \text{if } t \leq 0 \\ 1 & \text{otherwise} \end{cases} \quad (54)$$

$$f_1(t) = \begin{cases} 0 & \text{if } t \leq 0 \\ \frac{t}{T} & \text{if } 0 \leq t \leq T \\ 1 & \text{otherwise} \end{cases} \quad (55)$$

$$f_2(t) = \begin{cases} 0 & \text{if } t \leq 0 \\ \frac{1}{2}\left(1-\cos\left(\frac{\pi t}{T}\right)\right) & \text{if } 0 \leq t \leq T \\ 1 & \text{otherwise} \end{cases} \quad (56)$$

where $f_1(t)$ and $f_2(t)$ are used to make the loading smoothly achieve the steady value σ^* to decrease the numerical oscillations in the step loading $f_0(t)$. $T = 0.2t_c$ is chosen in the following. Here we are interested in the dynamic stress intensity factors denoted by K_I for the different loadings. Thus K_I^n denotes the

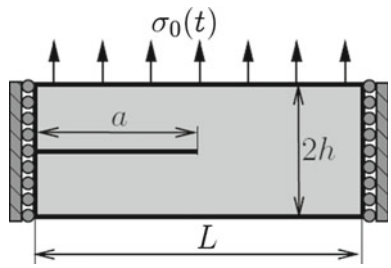

Fig. 8 Geometry and loading of the semi-infinite plate example

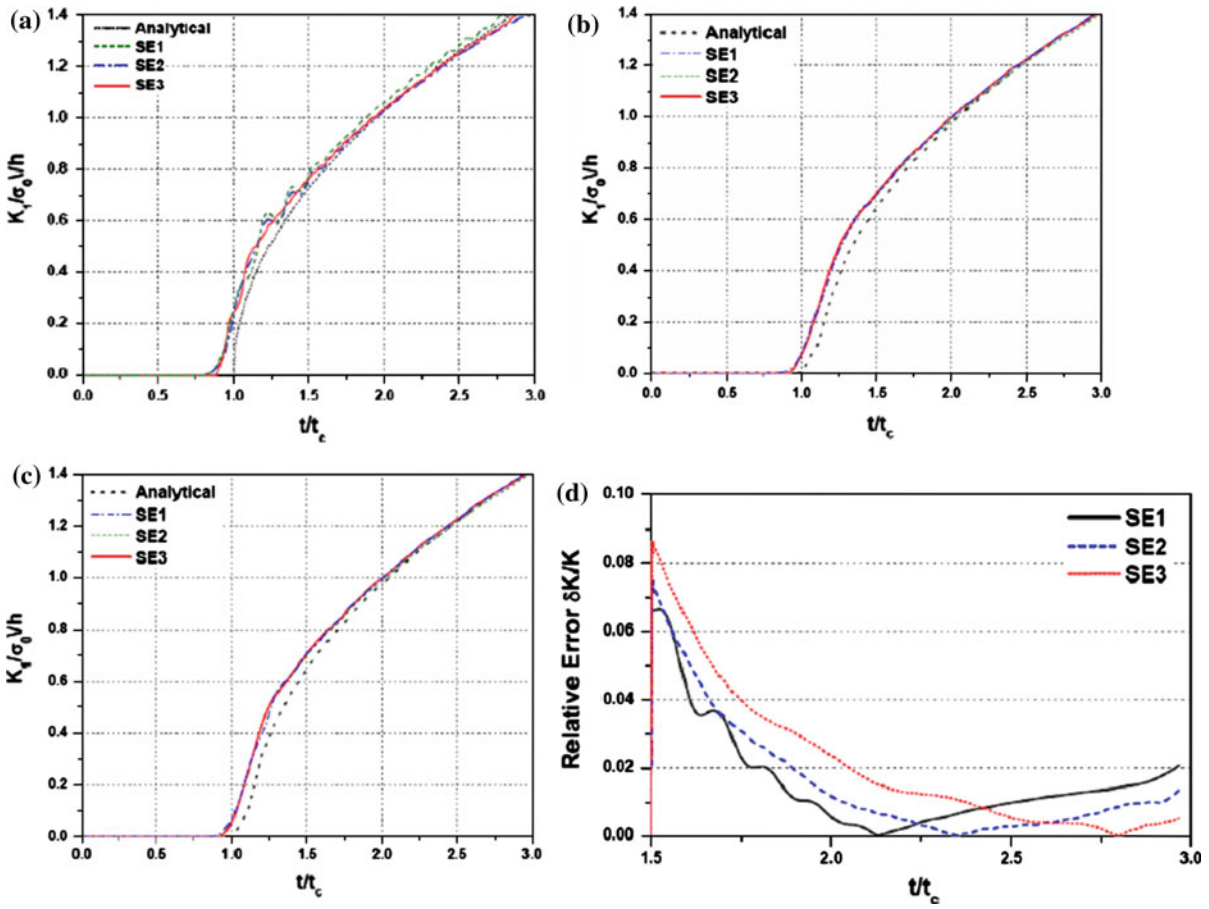

Fig. 9 Normalized mode 1 stress intensity factor as a function of time: analytical and numerical results for **a** loading $n = 0$ **b** loading $n = 1$ **c** loading $n = 2$ **d** relative error during $1.5t_c < t < 3t_c$ for loading $f_2(t)$

dynamic stress intensity factor for the loading n ($n = 0, 1, 2$).

Two different simulations are reported here: the first one with a stationary crack and the second one with a moving crack driven by an imposed velocity of the crack tip. The stress intensity factor depends on time t and crack speed $\dot{a}$.

The theoretical dynamic stress intensity factor of this problem for step loading $n = 0$ is given by Freund (1990)

$$K_I^0(\dot{a}, t) = K_I^0(0, t)k(\dot{a}) \tag{57}$$

where $K_I^0(0, t)$ is the stress intensity factor for $\dot{a} = 0$. As the tensile wave reaches the crack at time t_c it can be written as:

$$K_I^0(0, t) = \begin{cases} 0 & t < t_c \\ \frac{2\sigma^*}{1-\nu}\sqrt{\frac{c_1(t-t_c)(1-2\nu)}{\pi}} & t \geq t_c \end{cases} \tag{58}$$

The function $k(\dot{a})$ can be written as:

$$k(\dot{a}) = \frac{1 - \frac{\dot{a}}{c_r}}{\sqrt{1 - \frac{\dot{a}}{c_1}}} \tag{59}$$

where the Rayleigy wave speed $c_r = 2,947\,\text{m/s}$, dilatational wave speed $c_1 = 5,944\,\text{m/s}$.

The analytical dynamic stress intensity factor $K_I^n(0, t)$ for other loadings can be obtained with the convolution theory as:

$$K_I^n(0, t) = \int_{-\infty}^{\infty} \sigma_0(t - \tau)g(\tau)d\tau \tag{60}$$

where g is the stress intensity factor correspond to an impulse load, and $\sigma_0(t) = \sigma^* f_n(t)$. From this equation, all the different results can be explicitly developed as a function of the loading, crack speed and time. The details for the calculations are given in the appendix.

The dynamic stress intensity factor $K_I^n(0,t)$ also can be calculated using Ravi Chandar theory (Ravi-Chandar 2004) as

$$K_I^n(0,t) = \int_0^t K_I^0(0,t-\tau)\dot{f}_n(\tau)d\tau \tag{61}$$

where the stress intensity factor K_I^0 corresponds to the step loading $n = 0$. $\dot{f}_n$ denotes the derivative of f_n with time.

6.1.1 Stationary crack

Figure 9a, b, c present the normalized stress intensity factors as a function of time under three different loadings. The stress intensity factors are normalized by $\sigma^*\sqrt{h}$ and compared for element SE1, SE2 and SE3. For the step loading $f_0(t)$ in Fig. 9a, one can notice that apparent numerical oscillations appear in the stress intensity factor for element SE1. This was also observed in the same simulations carried out by the other researchers using low-order element (Elguedj et al. 2009; Menouillard et al. 2006, 2010). However, for element SE2 and SE3, the stress intensity factors vary smoothly when the tensile wave and the reflected wave approach the crack tip, and the results are quite similar to the analytical results. The error near $t = t_c$ is due to the tensile wave entering the contour for the stress intensity factor computation. For smooth loading $f_1(t)$ and $f_2(t)$, the error near $t = t_c$ is decreased as shown in Fig. 9b and c. Especially for element SE1, the oscillations markedly decrease when the tensile wave arrives at the crack tip as shown in Fig. 9b and c. The relative errors during $1.5t_c < t < 3t_c$ for loading $f_2(t)$ are given in Fig. 9d.

Increasing mesh density is another method to improve the finite element results. Next the effects of refining mesh and increasing element order on the results are compared to further explore the character of this spectral XFEM method. A coarse mesh of 39×78 is used in this investigation. The contours of stress S_{yy} near crack tip at $t = 3t_c$ for different element types and mesh densities are given in Fig. 10. It is p-refinement from left to right and h-refinement from top to bottom.

We can find that for low-order element SE1, refining mesh cannot apparently decrease the stress oscillations below the crack surface, see the diagrams in the first column of Fig. 10. For element SE3, the stress oscillations near the crack tip are effectively suppressed both for the coarse and fine meshes. It seems p-refinement is more effective on improving the numerical noise near the crack tip than h-refinement.

6.1.2 Moving crack

Next we study the effect of moving crack on the accuracy of the computed stress intensity factor and verify the performance of spectral element in the simulation of

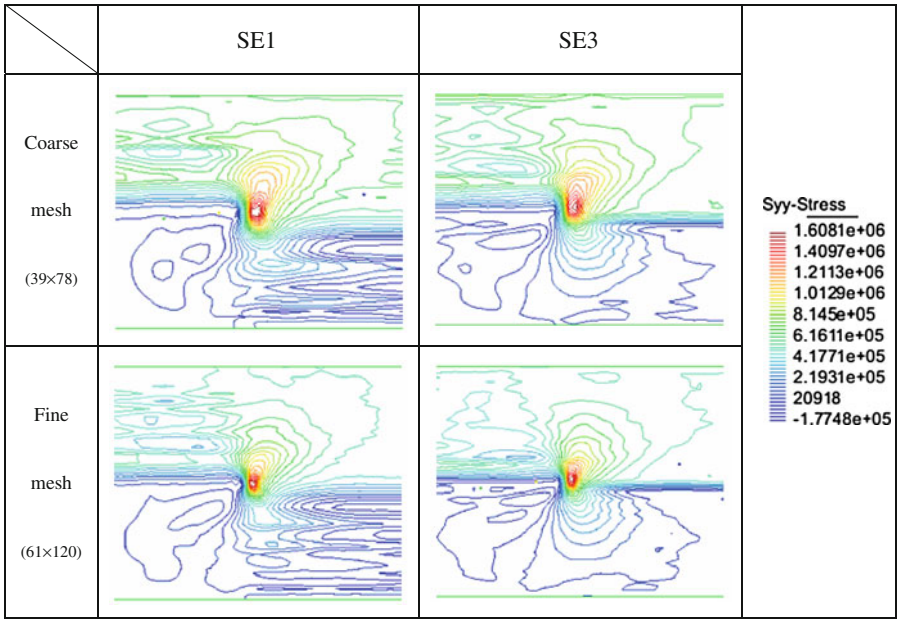

Fig. 10 Comparison of stress contour near crack tip at $t = 3t_c$ for element SE1 and SE3 with different mesh densities

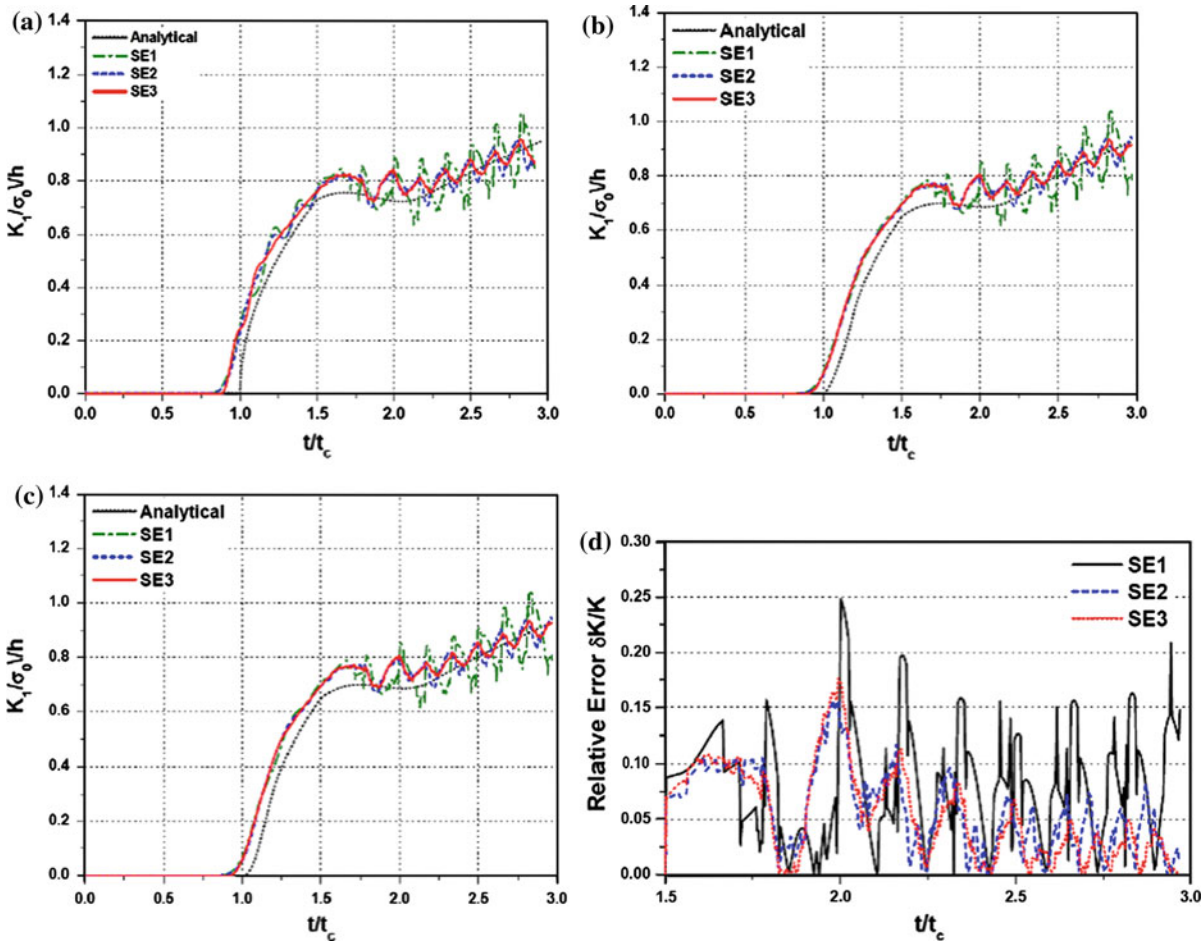

Fig. 11 Normalized mode 1 stress intensity factors as a function of time: analytical and numerical results for **a** loading $n = 0$ **b** loading $n = 1$ **c** loading $n = 2$ **d** relative error during $1.5t_c < t < 3t_c$ for loading $n = 2$

dynamic crack propagation. A smoothed crack velocity is imposed after $1.5t_c$ as given below

$$\dot{a} = \begin{cases} 0 & t < 1.5t_c \\ V_0 \sin\left[\frac{(t-1.5t_c)\pi}{1.4t_c}\right] & 1.5t_c \leq t \leq 2.2t_c \\ V_0 & t > 2.2t_c \end{cases} \quad (62)$$

where $V_0 = 1,500\,\mathrm{m/s}$.

Figure 11a, b, c present the normalized stress intensity factors as a function of time under three different loadings. The stress intensity factors are normalized by $\sigma^*\sqrt{h}$ and compared for element SE1, SE2 and SE3. As shown in Fig. 11, the numerical oscillations during the crack propagation are strongly amplified in element SE1 for the three loadings. However, the stress wave due to releasing tip element is effectively decreased in element SE2 and SE3. Figure 11d presents the relative error on the stress intensity factor corresponding to the result shown in Fig. 11c. It underlines the spectral element markedly improve the results. The small oscillations in element SE2 and SE3 correspond to the crack tip passing from one element to the next. This error was also apparent in the time-dependent tip enrichment technique in References Elguedj et al. (2009), Menouillard et al. (2010), Réthoré et al. (2005).

The stress contour at $t = 3t_c$ for element SE1 and SE3 are given in Fig. 12, respectively. The crack-tip stress field distribution in element SE1 is strongly disordered by wave oscillations during the crack propagation as shown in Fig. 12. That is why large oscillations appear in the stress intensity factor of element SE1, see Fig. 11. This example evidently demonstrates the

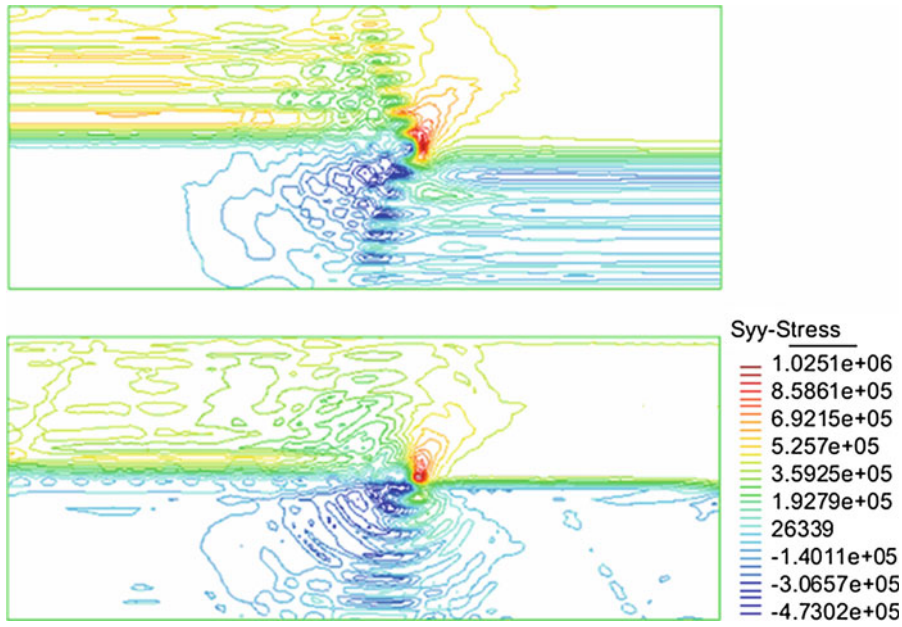

Fig. 12 Stress contour at $t = 3t_c$ for loading $n = 0$: the upper for element SE1 and the bottom for element SE3

improvement of spectral element in the simulation of dynamic crack propagation.

6.2 Mixed mode crack

In this section we consider the problem analyzed by Lee and Freund (1990) in which a semi infinite plate with an edge notch is subjected to an impact velocity V_0. The problem is mixed mode due to the traction free nature on the crack faces. The mode I stress intensity factor becomes negative when the lower part of the specimen comes in contact with the upper part.

The geometry of the finite plate is shown in Fig. 13. The dimensions are the following: $H = 6\,\text{m}$, $L = 4\,\text{m}$, the crack length $a = 1\,\text{m}$. A mesh of 60×119 spectral elements is used to define the model. The prescribed velocity on the boundary is $V_0 = 16.5\,\text{m/s}$. Since the analytical solution is for an infinite plate, it is only valid for a finite plate until the reflected wave arrived at the crack tip. Therefore in our numerical solution we limit the simulation time to $t \leq 3t_c = 3a/c_1$, where c_1 is dilatational wave speed. The material properties of the linear elastic media are: Young's modulus $E = 200\,\text{GPa}$, Poisson's ratio $\nu = 0.25$ and the density $\rho = 7833\,\text{kg/m}^3$. The stress intensity factors are normalized by the factor $\frac{-EV_0\sqrt{a/\pi}}{2c_1(1-\nu^2)}$. The analytical solution for both stress intensity factors as a function of time is available for this problem (Lee and Freund 1990).

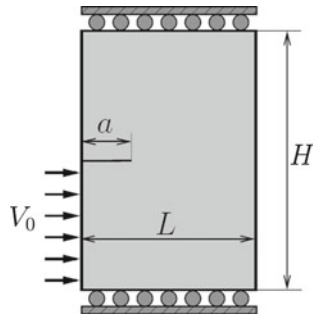

Fig. 13 Semi-infinite plate with a stationary edge crack under mixed-mode loading

Figure 14 presents the normalized stress intensity factors K_I and K_{II} as a function of time for element SE1 and SE3. We can find that the element SE3 performs well during the whole loading history. In contrast, the results for element SE1 strongly deviate from the analytical results especially, at the late stages of the simulation. The high-order spectral element is more accurate than the low-order element for this mixed mode crack problem.

6.3 Kalthoff's experiment

This example is based on the experiment of Kalthoff (1985) and by Böhme and Kalthoff (1982) and deals with the crack initially in mode 2. A plate with two

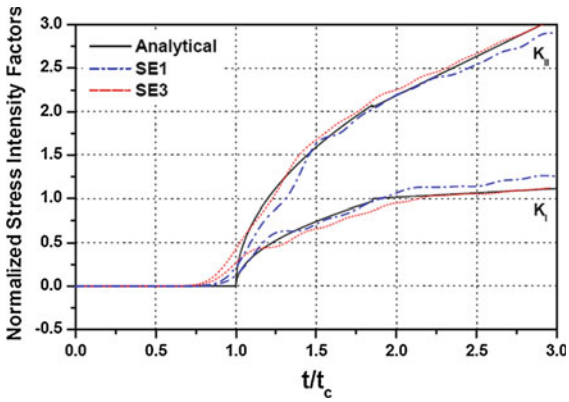

Fig. 14 Normalized stress intensity factors as a function of time: analytical and numerical results

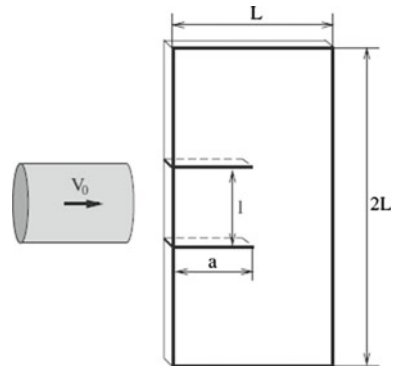

Fig. 15 Geometry of the Kalthoff's experiment

symmetrical edge cracks is impacted by a projectile at speed V_0. The two cracks are centered with respect to the specimen's geometry and their separation corresponds to the diameter of the projectile. The crack propagates with an overall angle from 60° to 70°. We chose $V_0 = 16.5$ m/s as a typical velocity for brittle fracture. A schematic description of the problem and the geometry is given by Fig. 15. The dimension of the specimen are: $L = 100$ mm, $l = 50$ mm, $a = 50$ mm and the thickness is 16.5 mm. The material properties of the linear elastic media are: Young's modulus $E = 190$ GPa, Poisson's ratio $\nu = 0.3$, the density $\rho = 8,000\,\text{kg/m}^3$ and fracture toughness $K_{IC} = 68\,\text{MPa}\sqrt{\text{m}}$. This problem is widely used to validate numerical methods in dynamic crack propagation.

Regular meshes (38×38, 78×78) were employed in the simulations. The crack velocity is driven by Eq. (52).

Figure 16 shows the result for the fine mesh 78×78. It can be seen that crack paths for element SE2 and SE3 are almost identical, thus that path can be considered as a converged solution. The angle is close to 70°.

The results for the coarse mesh 38×38 are given in Fig. 17a. The crack path of high-order element SE3 still closely follows a 70° angle, though not as smoothly as that of fine mesh. The crack paths for different element meshes and element orders are compared in Fig. 17b together. We can find that the crack path of element SE3 in the coarse mesh is even more accurate than that of element SE1 in the fine mesh.

7 Conclusion

A high-order extended finite element (XFEM) method based on spectral elements (SE) has been developed to improve the accuracy in the simulation of dynamics fractures. The partitions of unity for the discontinuous displacement are constructed by employing p order spectral element. The well known form of the explicit central difference scheme is used and the critical time step for this method is investigated. We find that by

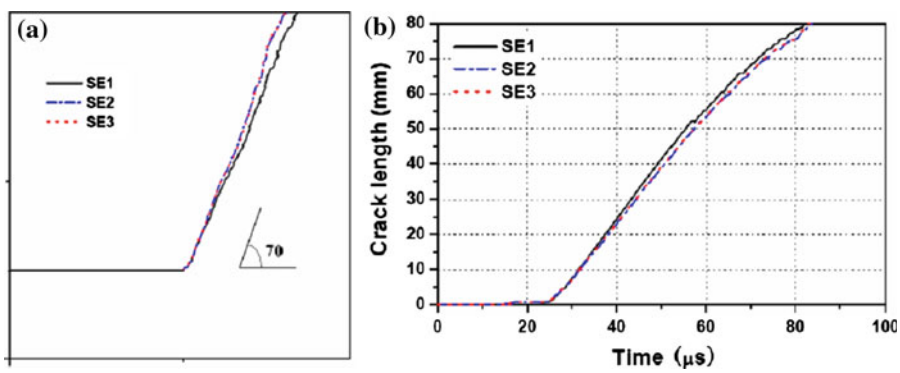

Fig. 16 **a** Crack paths and **b** Crack lengths of the Kalthoff test for element mesh 78×78

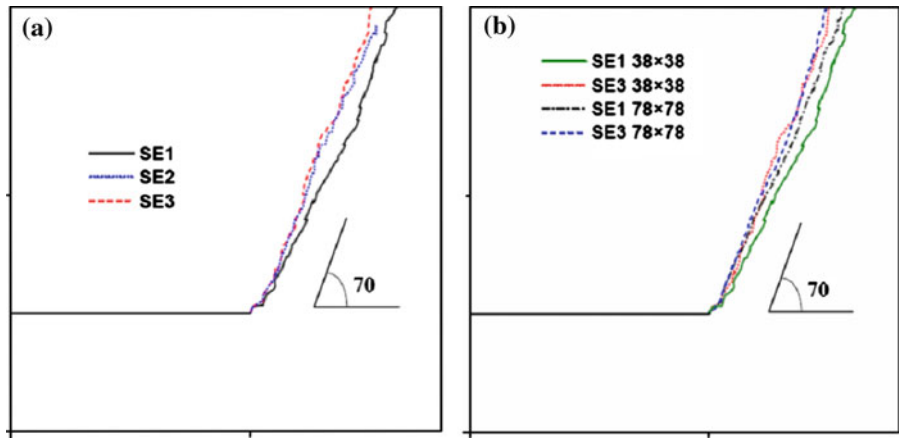

Fig. 17 **a** Crack paths and for element mesh 38 × 38. **b** Comparison of crack paths for different element meshes and element orders

using lumped mass matrix the critical time step Δt_c for this high-order extended finite element is almost independent of the crack position. This method shows great advantages in the simulations of moving crack and mixed mode crack. The numerical oscillations are effectively suppressed and the accuracy of computed stress intensity factors and crack path are improved markedly. Furthermore the simulation results show that p-refinement is more effective in improving the stress contour near the crack tip than h-refinement. The methodology is promising for a wide variety of applications involving dynamic fracture problems.

Acknowledgments The support of the Office of Naval Research under Grants N00014-08-1-1191 and N00014-09-1-0030 and also the Army Research Office under Grant W911NF-008-1-0212 is gratefully acknowledged.

Appendix

For a moving crack, the dynamics stress intensity factor $K_I^n(t, \dot{a})$ is related to the one corresponding to the stationary crack $K_I^0(t, 0)$ modified by a function k depending on the crack speed $\dot{a}$ as follows:

$$K_I^n(\dot{a}, t) = K_I^n(0, t)k(\dot{a}) = K_I^n(t)\frac{1 - \frac{\dot{a}}{c_r}}{\sqrt{1 - \frac{\dot{a}}{c_1}}} \tag{A1}$$

where c_r denotes the Rayleigy wave speed, c_1 denotes dilatational wave speed.

The dynamic stress intensity factor can be obtained with the convolution theory as:

$$K_I^n(0, t) = \int_{-\infty}^{\infty} \sigma_0(t - \tau)g(\tau)d\tau \tag{A2}$$

where $\sigma_0(t) = \sigma^* f_n(t)$, and g is the stress intensity factor corresponding to an impulse load:

$$g(t) = \frac{\alpha}{2\sqrt{t}}\sqrt{c_1} \tag{A3}$$

where $\alpha = \frac{2}{1-\nu}\sqrt{\frac{1-2\nu}{\pi}}$.

By substituting loading function f_n into Eq. (A2), the analytical dynamic stress intensity factor $K_I^n(t)$ for different loadings can be explicitly developed as a function of the loading, crack speed and time.

(i) Ramp loading: $n = 1$

$$\tilde{K}_I^1(0, t) = \frac{K_I^1(0, t)}{\alpha\sigma^*\sqrt{h}} = \frac{2}{3}\sqrt{\frac{T}{t_c}}\begin{cases} \left(\frac{t}{T}\right)^{3/2} & 0 \le t < T \\ \left(\frac{t}{T}\right)^{3/2} - \left(\frac{t}{T} - 1\right)^{3/2} & \text{otherwise} \end{cases} \tag{A4}$$

(ii) Cosinus loading $n = 2$

For $t \le T$:

$$\tilde{K}_I^2(0, t) = \frac{K_I^2(0, t)}{\alpha\sigma^*\sqrt{h}} = \frac{1}{2}\sqrt{\frac{t}{t_c}} - \frac{1}{4}\sqrt{\frac{2T}{t_c}}\left(\cos\left(\frac{\pi t}{T}\right) Fc\left(\sqrt{\frac{2t}{T}}\right) + \sin\left(\frac{\pi t}{T}\right) Fc\left(\sqrt{\frac{2t}{T}}\right)\right) \tag{A5}$$

and for $t > T$

$$\tilde{K}_I^2(0,t) = \frac{1}{2}\sqrt{\frac{t-T}{t_c}} + \frac{1}{2}\sqrt{\frac{t}{t_c}} - \frac{1}{4}\sqrt{\frac{2T}{t_c}}\cos\left(\frac{\pi t}{T}\right)\left[Fc\left(\sqrt{\frac{2t}{T}}\right) - Fc\left(\sqrt{\frac{2(t-T)}{T}}\right)\right] - \frac{1}{4}\sqrt{\frac{2T}{t_c}}\sin\left(\frac{\pi t}{T}\right)\left[Fs\left(\sqrt{\frac{2t}{T}}\right) - Fs\left(\sqrt{\frac{2(t-T)}{T}}\right)\right] \quad \text{(A6)}$$

where the Fresnel functions are defined by:

$$Fc(x) = \int_0^x \cos\left(\frac{\pi t^2}{2}\right)dt \quad \text{(A7)}$$

$$Fs(x) = \int_0^x \sin\left(\frac{\pi t^2}{2}\right)dt \quad \text{(A8)}$$

References

Areias P, Belytschko T (2005) Analysis of three-dimensional crack initiation and propagation using the extended finite element method. Int J Numer Meth Eng 63:760–788

Attigui M, Petit C (1997) Mixed-mode separation in dynamic fracture mechanics: new path independent integrals. Int J Fract 84:19–36

Belytschko T, Black T (1999) Elastic crack growth in finite elements with minimal remeshing. Int J Numer Meth Eng 45:601–620

Belytschko T, Chen H, Xu J, Zi G (2003) Dynamic crack propagation based on loss of hyperbolicity and a new discontinuous enrichment. Int J Numer Meth Eng 58:1873–1905

Belytschko T, Liu W, Moran B (2000) Nonlinear finite elements for continua and structures. Wiley, New York

Böhme W, Kalthoff J (1982) The behavior of notched bend specimens in impact testing. Int J Fract 20:139–143

Capdeville Y, Chaljub E, Vilotte J, Montagner J (2003) Coupling the spectral element method with a modal solution for elastic wave propagation in global Earth models. Geophys J Int 152:34–67

Chessa J, Wang H, Belytschko T (2003) On the construction of blending elements for local partition of unity enriched finite elements. Int J Numer Meth Eng 57:1015–1038

Duan Q, Song J, Menouillard T, Belytschko T (2009) Element-local level set method for three-dimensional dynamic crack growth. Int J Numer Meth Eng 80:1520–1543

Elguedj T, Gravouil A, Maigre H (2009) An explicit dynamics extended finite element method. Part 1: mass lumping for arbitrary enrichment functions. Comput Meth Appl Mech Eng 198:2297–2317

Fish J, Belytschko T (1990) A finite element with a unidirectionally enriched strain field for localization analysis. Comput Meth Appl Mech Eng 78:181–200

Fleming M, Chu Y, Moran B, Belytschko T, Lu Y, Gu L (1997) Enriched element-free Galerkin methods for crack tip fields. Int J Numer Meth Eng 40:1483–1504

Freund L (1990) Dynamic fracture mechanics. Cambridge University Press, Cambridge

Freund L, Douglas A (1982) The influence of inertia on elastic-plastic antiplane-shear crack growth. J Mech Phys Solids 30:59–74

Hansbo A, Hansbo P (2004) A finite element method for the simulation of strong and weak discontinuities in solid mechanics. Comput Meth Appl Mech Eng 193:3523–3540

Kalthoff J (1985) On the measurement of dynamic fracture toughnesses-areview of recent work. Int J Fract 27:277–298

Karniadakis G, Sherwin S (1999) Spectral/hp element methods for CFD. Oxford University Press, USA

Komatitsch D, Tromp J (1999) Introduction to the spectral element method for three-dimensional seismic wave propagation. Geophys J Int 139:806–822

Komatitsch D, Vilotte J (1998) The spectral element method: an efficient tool to simulate the seismic response of 2D and 3D geological structures. Bull Seismol Soc Am 88:368–392

Krysl P, Belytschko T (1999) The element free Galerkin method for dynamic propagation of arbitrary 3-D cracks. Int J Numer Meth Eng 44:767–800

Lee Y, Freund L. (1990) Fracture initiation due to asymmetric impact loading of an edge cracked plate. J Appl Mech 57:104–111

Legay A, Wang H, Belytschko T (2005) Strong and weak arbitrary discontinuities in spectral finite elements. Int J Numer Meth Eng 64:991–1008

Melenk J, Babuška I (1996) The partition of unity finite element method: basic theory and applications. Comput Meth Appl Mech Eng 139:289–314

Menouillard T, Belytschko T (2009) Correction Force for releasing crack tip element with XFEM and only discontinuous enrichment. Eur J Comput Mech 18:465–483

Menouillard T, Belytschko T (2010) Dynamic fracture with meshfree enriched XFEM. Acta Mech 213:53–69

Menouillard T, Réthoré J, Combescure A, Bung H (2006) Efficient explicit time stepping for the extended finite element method (X-FEM). Int J Numer Meth Eng 68:911–939

Menouillard T, Réthoré J, Moës N, Combescure A, Bung H (2008) Mass lumping strategies for X-FEM explicit dynamics: application to crack propagation. Int J Numer Meth Eng 74:447–474

Menouillard T, Song J, Duan Q, Belytschko T (2010) Time dependent crack tip enrichment for dynamic crack propagation. Int J Fract 162:33–49

Mercerat E, Vilotte J, Sanchez-Sesma F (2006) Triangular spectral element simulation of two-dimensional elastic wave propagation using unstructured triangular grids. Geophys J Int 166:679–698

Moës N, Dolbow J, Belytschko T (1999) A finite element method for crack growth without remeshing. Int J Numer Meth Eng 46:131–150

Padovani E, Priolo E, Seriani G (1994) Low-and high-order finite element method: experience in seismic modeling. J Comput Acoust 2:371–422

Patera A (1984) A spectral element method for fluid dynamics: laminar flow in a channel expansion. J Comput Phys 54:468–488

Ravi-Chandar K (2004) Dynamic fracture. Elsevier, Amsterdam

Réthoré J, Gravouil A, Combescure A (2005) An energy-conserving scheme for dynamic crack growth using the extended finite element method. Int J Numer Meth Eng 63:631–659

Rice J (1968) A path independent integral and the approximate analysis of strain concentration by notches and cracks. J Appl Mech 35:379–386

Rosakis A, Freund L (1982) Optical measurement of the plastic strain concentration at a crack tip in a ductile steel plate. J Eng Mater Technol 104:115

Seriani G, Oliveira S (2007) Dispersion analysis of spectral element methods for elastic wave propagation. Wave Motion 45:729–744

Song J, Areias P, Belytschko T (2006) A method for dynamic crack and shear band propagation with phantom nodes. Int J Numer Meth Eng 67:863–893

Song J, Belytschko T (2009) Dynamic fracture of shells subjected to impulsive loads. J Appl Mech 76:051301